Accurate Identification of Seed Maize Fields Based on Histogram of Stripe Slopes

Yunqi Shen, Hongyan Wang, Yuan Zhang, Xin Du, Qinghan Dong, Qiangzi Li, Yueting Wang, Sichen Zhang, Yong Dong, Jing Xiao, Jingyuan Xu, Sifeng Yan, Shuguang Gong, and Haoxuan Hu

***Abstract*—In China, the process of emasculation of seed maize usually occurs in August. To prevent self-pollination by removing the tassels from every few rows of maize and to ensure the production of high-quality hybrid maize seeds, resulting in the formation of distinctive stripe-like textural features that show up in high-resolution satellite images. These features can be used as distinctive features to differentiate seed maize fields from common maize fields. In this study, Beijing-3A1 satellite image data with a resolution of 0.5 m were used to identify seed maize fields in Zhangye City, Gansu Province. First, the extraction of maize plots in remote sensing images is performed using a modified U^2-net with a new field boundary loss function. Second, a new feature named "histogram of stripe slopes (HoSS)" was developed for seed maize field classification. We compare the classification accuracy obtained using HoSS features with different classifiers using other conventional features. The results show that HoSS features exhibit superiority for both single-feature classification and feature set classification. The feature set including entropy and HoSS with the K-nearest neighbor classification model as the method chosen in this study achieved 93.7% accuracy in identifying seed maize fields.**

***Index Terms*—Improved U^2-net, parcel segmentation, seed maize, seed maize field identification.**

Received 23 January 2024; revised 27 March 2024, 21 May 2024, and 1 July 2024; accepted 27 July 2024. Date of publication 21 August 2024; date of current version 15 October 2024. This work was supported in part by the Key Program of the Institute under Grant E2Z211020F, in part by the National Key R&D Program of China under Grant 2021YFD1500103, in part by the National Science Foundation of China under Grant 42071403, in part by the Strategic Priority Research Program of the Chinese Academy of Sciences under Grant XDA28070504, and in part by the Key Program of High-resolution Earth Observation System under Grant 00-Y30B01-9001-22/23-CY-10. *(Corresponding authors: Hongyan Wang; Qiangzi Li.)*

Yunqi Shen, Sichen Zhang, Yong Dong, Jing Xiao, Jingyuan Xu, Sifeng Yan, Shuguang Gong, and Haoxuan Hu are with the Aerospace Information Research Institute, Chinese Academy of Sciences, Beijing 100094, China, and also with the University of Chinese Academy of Sciences, Beijing 100049, China (e-mail: shenyunqi21@mails.ucas.ac.cn; zhangsichen211@mails.ucas.ac.cn; dongyong22@mails.ucas.ac.cn; xiaojing221@mails.ucas.ac.cn; xujingyuan22@mails.ucas.ac.cn; yansifeng23@mails.ucas.ac.cn; gongshuguang23@mails.ucas.ac.cn; huhaoxuan23@mails.ucas.ac.cn).

Hongyan Wang, Yuan Zhang, Xin Du, and Yueting Wang are with the Aerospace Information Research Institute, Chinese Academy of Sciences, Beijing 100094, China (e-mail: wanghy@aircas.ac.cn; zhangyuan@aircas.ac.cn; duxin@aircas.ac.cn; wangyueting@aircas.ac.cn).

Qinghan Dong is with the Department of Remote Sensing, Aerospace Information Research Institute, Flemish Institute of Technological Research, 2400 Mol, Belgium (e-mail: qinghan.dong@vito.be).

Qiangzi Li is with the Aerospace Information Research Institute, Chinese Academy of Sciences, Beijing 100094, China, also with the University of Chinese Academy of Sciences, Beijing 100049, China, and also with the College of Environment and Planning, Henan University, Kaifeng 475004, China (e-mail: liqz@aircas.ac.cn).

Digital Object Identifier 10.1109/JSTARS.2024.3441644

I. Introduction

THE production of seed maize plays a vital role in ensuring the breeding and supply of new varieties. [1]. The seed industry is closely related to other industries in the development of globalization [2]. Accurate monitoring of the area and distribution of seed corn is an important part of safe agricultural production, which used to be time-consuming and labor-intensive through manual field surveys. Remote sensing provides the ability to monitor large areas [3], especially in the domain of agriculture [4]. Remote sensing monitoring is efficient and accurate and is the mainstream direction for future seed corn identification.

From our knowledge, studies on the identification of seed maize fields remain in some way limited. The identification methods can be categorized into two groups: The one-step method for identifying seed-producing maize plots in remote sensing images by using pixel-scale features. Some researchers used time-series features of texture features for seed maize field recognition, whereas some researchers used a random forests model combined with spectral and texture features to directly identify seed maize fields [5]. Ren et al. [6] simply used the temporal profiles of some vegetation indices to identify seed maize fields. However, since the differences between seed maize fields and common maize fields are mainly in texture, the traditional one-step classification method mainly relies on pixel-level classification, which is unable to capture the overall block-level texture features, resulting in a low classification accuracy [7]. To use block-level features for seed maize field recognition, some researchers have used a two-step classification approach, where the segmentation of the maize field is performed first, followed by recognition. In a study, maize fields were first extracted, and seed maize fields were then identified by the Sobel operator and the Hough transform [8]. Some scholars also designed a method based on an augmented vegetation index and decision trees model to segment maize plots and used the gray-level co-occurrence matrix (GLCM) to identify seeded maize fields [9].

All of the above methods utilize existing textural and spectral features for classification. However, it is difficult for these features to effectively extract the differences between seed maize fields and the common maize fields. The most notable difference between seed maize fields and common maize fields is the presence of visible striped texture patterns in the remote sensing imagery after detasseling [9], and distinguishing between seed maize fields and common maize fields relies on the classification of texture-related features [10]. There is still a lack of features

specifically designed for striped texture recognition. Considering that only one type of maize will be planted in a piece of arable land, identifying two types of maize at the sample scale can avoid confusion of the two types of maize and effectively improve the accuracy, but how the accuracy of the plot boundaries can be improved is also an important issue, the accuracy of field identification can be influenced by the precise prediction of cornfield boundaries. Currently, segmentation models often encounter issues with boundary adhesion when segmenting land parcels, resulting in the inability to obtain independent parcel extraction results. How to minimize this phenomenon remains to be resolved.

To address the aforementioned issues, this study adopted a two-step approach, utilizing an improved U^2-net model to segment maize fields [11], the U^2-net model works well in image segmentation [12], [13], [14], and a feature named "histogram of stripe slopes (HoSS)" designed for seed maize field recognition. The main contributions and novelties are summarized as follows.

1) We optimized its ability to segment the boundary by introducing a boundary loss function.
2) A feature named HoSS was specifically designed to recognize stripe features and outperform classical features in both machine learning and deep learning classification tasks.

II. Methods

In this section, we first present the U^2-net model improved by a boundary loss function and lightweight convolutions, by which we identify and segment the maize plots. In addition, we devised a statistical texture feature named HoSS to identify seed maize and common maize fields.

A. Improvements to U^2-Net for Field Segmentation

We improve the U^2-net model by 1) introducing a new loss function for field extraction, and 2) replacing normal convolution with depthwise separable convolution [15].

The segmentation procedure involves splitting the image into 512×512 pixel blocks with 50% horizontal and vertical overlap between neighboring blocks. These blocks are then fed individually into a pre-trained U^2-net model for field boundary prediction. Due to the directional overlap, each pixel was actually predicted four times. Pixels that were predicted to field at least two out of the four times were considered as the final maize field area Fig. 1.

We limited the maximum output channels of the encoder network layer to 64 to reduce computational resources and prevent model overfitting.Fig. 2 shows the architecture of the network.

The cross-entropy loss function [11] was used in the original U^2-net. Bokhovkin and Burnaev proposed a loss function for the task of building boundary segmentation based on the F1 score [16], which allowed the model to obtain good boundary recognition ability. We draw on the thinking about boundary accuracy. A field boundary loss function for segmentation was proposed for the U^2-net model. The loss function combines

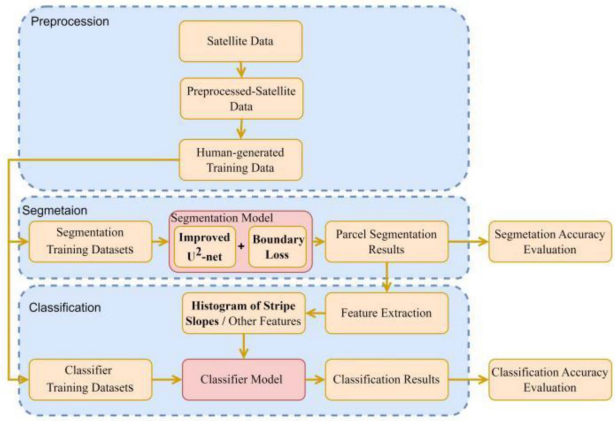

Fig. 1. Workflow for identifying seed maize fields.

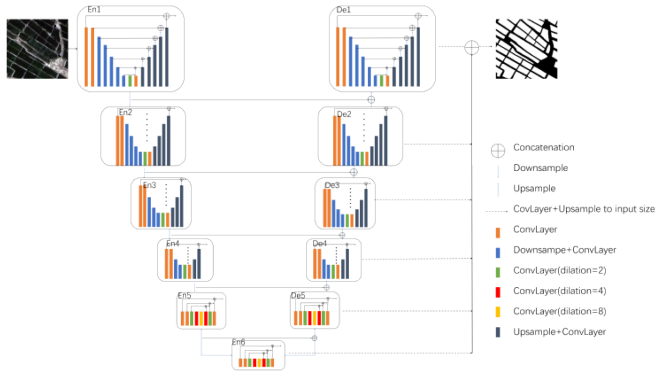

Fig. 2. Structure of U^2-net is based on U-net as a framework and a residual U block (RSU) is nested in each stage of U-net for feature extraction. The structure of RSU is similar to the U-net. The ConvLayer contains two layers of depthwise separable convolutions.

the cross-entropy of the image and the loss of the predicted boundary.

The dice loss function was used to evaluate the accuracy of the prediction result boundaries. Boundary parts of label data and predicted results are extracted by expansion and erosion operations.

$$\begin{cases} y_{gt}^{b} = \text{dilate}(y_{gt}) - \text{erode}(y_{gt}) \\ y_{pd}^{b} = \text{dilate}(y_{pd}) - \text{erode}(y_{pd}) \end{cases} \tag{1}$$

where y_{gt} represents the boundary of label data and y_{pd} represents the prediction boundary. Through morphological operations, we obtained the dilated region and the eroded region. Subtracting these two regions will give us the boundaries of the images. The real and predicted boundaries for maize fields are y_{gt}^{b} and y_{pd}^{b}.

Considering the small percentage of pixels that the boundary portion occupies in the overall image, the dice loss function [17] was used as the boundary loss function. This loss function makes the model exhibit good robustness in cases involving category

imbalance [18]

$$\begin{cases} \mathrm{DC} = 2 \times \frac{\mathrm{sum}(y_{gt}^{b} \cdot y_{pd}^{b})}{\mathrm{sum}(y_{gt}^{b}) + \mathrm{sum}(y_{pd}^{b})} \\ L_{\mathrm{dice}} = 1 - \mathrm{DC} \end{cases} \tag{2}$$

where DC represents the dice coefficient and L_{dice} is the dice loss. Equation (2) represents the calculation formula for the dice loss function. DC is the union of the true boundary with the predicted boundary divided by the sum of the pixels of the predicted boundary and the true boundary.

$$\begin{cases} L_{\mathrm{dice}} = 1 - \mathrm{DC} \\ L_{\mathrm{ent}} = \frac{1}{N}\mathrm{sum}(y_{gt} \cdot \log(y_{pd}) + (1 - y_{gt}) \cdot \log(1 - y_{pd})) \, . \\ L_{\mathrm{total}} = wL_{\mathrm{ent}} + (1 - w)L_{\mathrm{dice}} \end{cases} \tag{3}$$

Equation (3) combines two loss functions and serves as the loss function used in this study, where L_{total} is the final loss. The variable w is set to 0.2 in this study.

To reduce the number of parameters of convolution, Sifre and Mallat [15] proposed a structure for depthwise separable convolution. The depthwise separable convolution was used to solve several problems of the U^2-net. On the one hand, due to the large number of stacked layers in the U^2-net, it was prone to over-fitting during training, and the depthwise separable convolution significantly reduced model parameters and effectively prevented over-fitting. On the other hand, the original model has a huge number of parameters, whereas it reduces the number of parameters of the model very well [19].

The depthwise separable convolution can be divided into two parts. The first part is depthwise convolution, the input image of size c×h×w is split into c separate h×w images, each of which is independently convolved using a c×3×3 convolution kernel. The outputs are merged to form a feature map of size c×h×w. The other part is pointwise convolution. In this part, the feature image obtained from the previous step is convolved with o separate 1×1 convolution kernels. In the end, o×h×w feature maps are obtained. As a result, the model achieves higher feature dimensions while reducing the parameter quantity compared to normal convolutional layers.

B. Histogram of Stripe Slopes for Seed Maize Field Identification

The key difference between the seed maize fields and the common maize fields is in the texture features. In seed maize fields, every 5 to 6 rows, one row of male reproductive organs (tassels) is removed. After the removal of the tassels, seed maize fields appeared as distinct stripe textures in the images (see Fig. 3). By extracting the stripe texture and analyzing the distribution of these stripes, it is possible to effectively distinguish between these two cornfield types. A statistical feature for stripe texture called HoSS was developed for this purpose.

The HoSS feature was proposed to identify the texture of the stripes by analyzing the distribution of the slope of the stripes in images. The HoSS feature combines the gradient features as well as the statistics of the slope distribution of the stripe connectivity region to enhance the recognition of the stripe texture in the image. The specific process is to calculate the gradient of each pixel of the image in the horizontal vertical direction

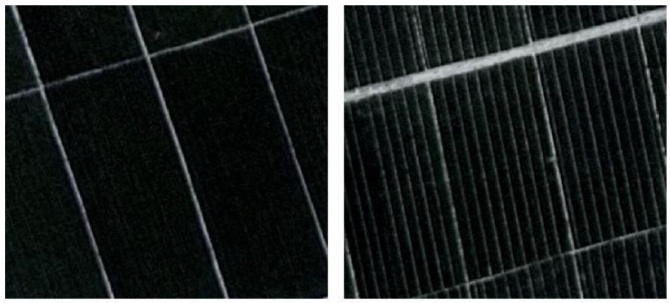

Fig. 3. Different textures were observed from (a) common maize fields and (b) seed maize fields where stripe texture was visible.

using the Sobel convolution kernel and the direction of the image gradient can be calculated by the inverse tangent function. Specific calculations are shown in (4)–(6). The image gradient direction was resampled into four directions: up, left, down, and right, with coordinate ranges of [π/4, 3π/4), [3π/4, 5π/4), [5π/4, 7π/4), and [7π/4, 9π/4), The distribution of gradient directions was then statistically analyzed and the two directions with the highest distributions were selected. These two directions should correspond to the distribution of striped regions if a striped texture is present. The regions were assigned values 1 and 2 according to the gradient direction, whereas other regions were assigned the value 0, forming the HoSS feature image as shown in Fig. 4(b).

$$\mathrm{Sobel}_y = \begin{pmatrix} 1 & 2 & 1 \\ 0 & 0 & 0 \\ -1 & -2 & -1 \end{pmatrix}, \quad \mathrm{Sobel}_x = \begin{pmatrix} 1 & 0 & -1 \\ 2 & 0 & -2 \\ 1 & 0 & -1 \end{pmatrix} \tag{4}$$

$$\begin{cases} G_y = \mathrm{Convolution}(\mathrm{Sobel}_y, \mathrm{Img}) \\ G_x = \mathrm{Convolution}(\mathrm{Sobel}_x, \mathrm{Img}) \end{cases} \tag{5}$$

$$\mathrm{Direction} = \arctan(G_y / G_x). \tag{6}$$

The image matrix is treated as a Cartesian coordinate system and straight lines are fitted to the connected regions in the image by least squares method, as shown in Fig. 4(c). We performed a statistical distribution analysis on the slopes, and the histogram of the slope distribution was created. The histogram was normalized to obtain the HoSS feature vector [see Fig. 4(d)]. To ensure that the feature vectors had rotational invariance, the order of the values in the feature vectors was adjusted so that the maximum value was located in the middle of the vector. In the classification task, the HoSS vector features were input to a machine learning classifier to identify the seed maize field. For the deep learning classifier, we input the HoSS feature images directly into the deep learning classifier to retain more features.

III. Experiments

A. Study Area and Datasets

Ganzhou District, Zhangye City, Gansu Province is one of the largest maize seed producers in China [20]. The study area covered the area located at 100.07° to 100.50°E longitude and

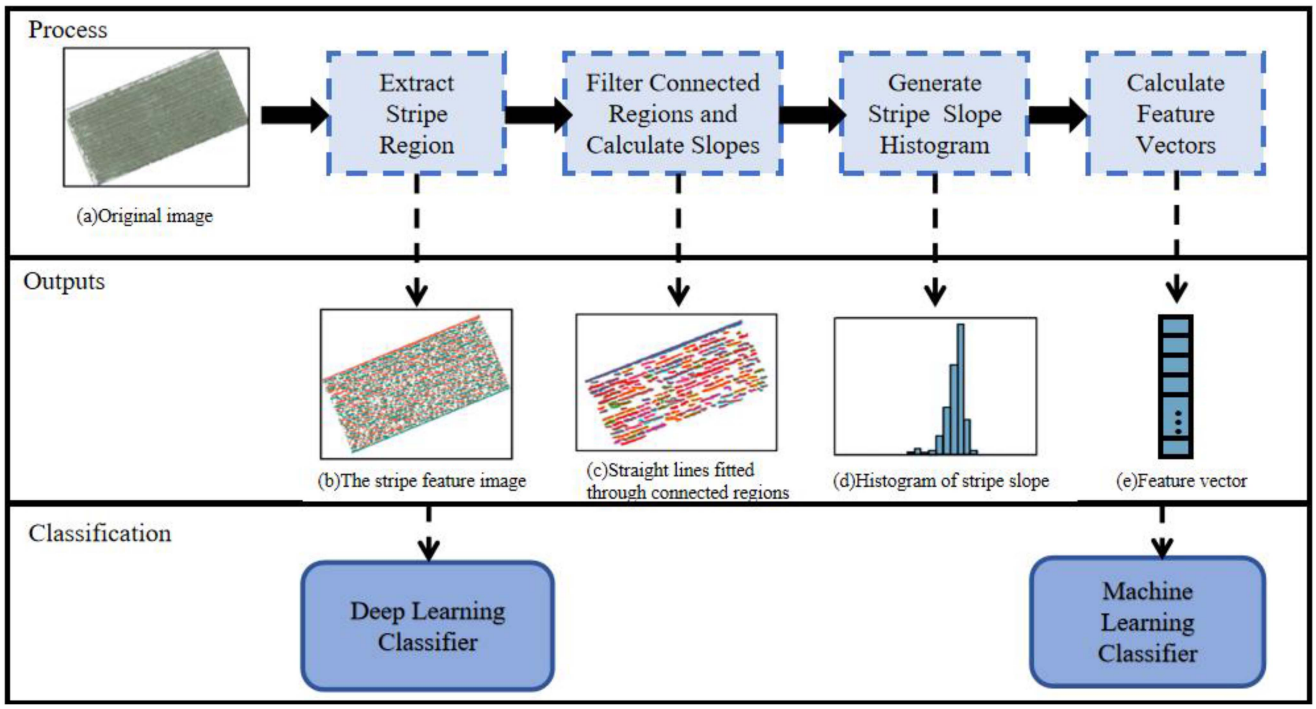

Fig. 4. Process of generating HoSS and applying it to the classifiers.

38.66° to 39.32°N latitude. The image coverage area is approximately 1900 square kilometers. The average altitude of this area is 1500 m above sea level, with a mean annual precipitation of 113–120 mm and a frost-free period of 138–179 days. The region is characterized by long sunshine hours (3085 h of sunshine per year) and a large temperature difference between day and night while providing a good growing environment for seed maize by virtue of its good agricultural infrastructure and convenient irrigation conditions [21]. Ganzhou District is our main study area. Additionally, we have included two more experimental areas to validate the effectiveness of this method, located in Huocheng County (80.6°E to 80.8°E, 44.0°N to 44.3°N), approximately 223 square kilometers in area and Qitai County (89.4° to 89.7°E, 43.5°N to 44.0°N), and approximately 552 square kilometers in area in Xinjiang Uygur Autonomous Region (see Fig. 5).

The data used for the experiments include the training set of segmentation and classification models produced from Beijing-3A remote sensing data, and this section develops a detailed description of the data.

The Beijing-3A (BJ-3A1) satellite data (see Table I) registered on August 5th, 2022, covering the study area has been used for this study (Krasovsky 1940 projection). Preprocessing including geometric and radiometric corrections was applied. We fused PAN-band data with multispectral data to obtain multispectral data with 0.5 m resolution and pixel values were converted to 8-bit format.

The training data consist of two training sets, i.e., segmentation and classification: the image segmentation dataset was used for the training of the maize plot extraction model, which includes remote sensing images and label data. Each image consists of four bands with a size of 512 × 512 and the corresponding label data are a binary image with a size of 512 × 512. The categories of the training set were only the maize and nonmaize categories, other features such as buildings, roads, and other crops were categorized as nonmaize categories: 1 for maize fields and 0 for other land uses. The original training set was formed by manually outlining the maize field labels of 621 images, which were expanded to 2484 training samples using techniques, such as image rotation and noise addition. Fig. 6(a) and (b) shows a set of images and corresponding label data. The classification dataset was used to train the maize plot classification model. The classification dataset consisted of maize plots with the categories of seed maize and common maize. The categories were determined by ground survey and visual interpretation. The survey was conducted in August 2022 in Ganzhou District. Eventually, we produced 1600 training samples, 800 each from seed maize fields and common maize

TABLE I
BJ-3A1 SATELLITE SENSOR PARAMETERS

Band number	Spectral region	Wavelength range (nm)	Spatial resolution (m)
1	Blue	450–520	2
2	Green	520–630	2
3	Red	630–690	2
4	NIR	770–890	2
5	PAN	450–700	0.5

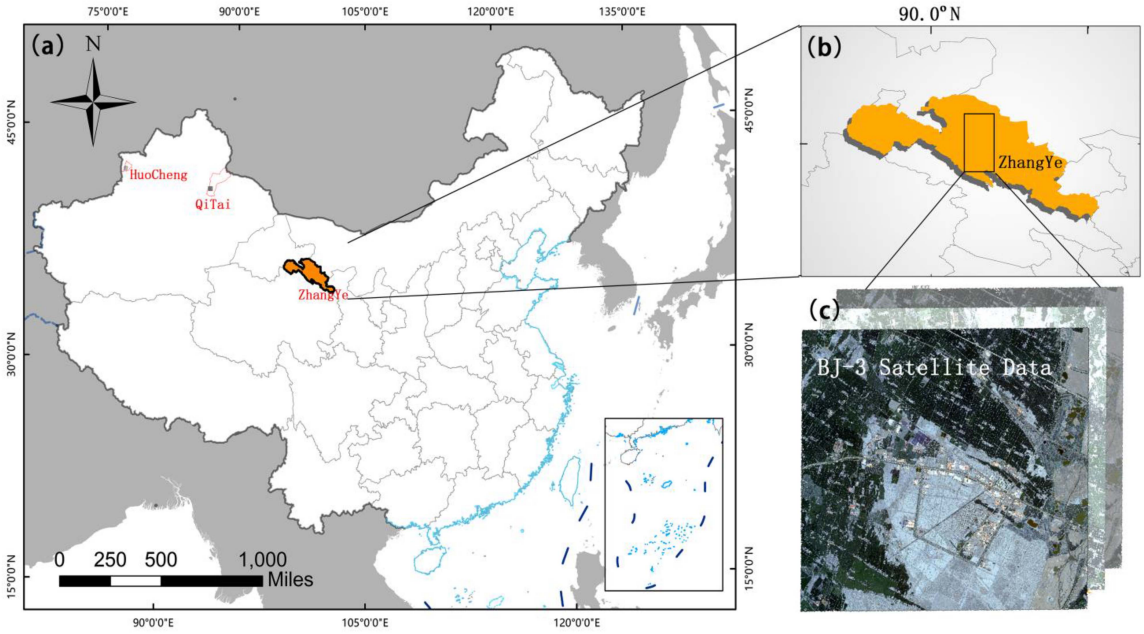

Fig. 5. Location of the study area (Ganzhou, Zhangye) and test area (Qitai and Huocheng). (a) Zhangye city. (b) Study region in Zhangye. (c) BJ-3A1 satellite image. The study area is used for training and validation of the model. The test area is solely used for validating the effectiveness in other corn planting areas and does not participate in training.

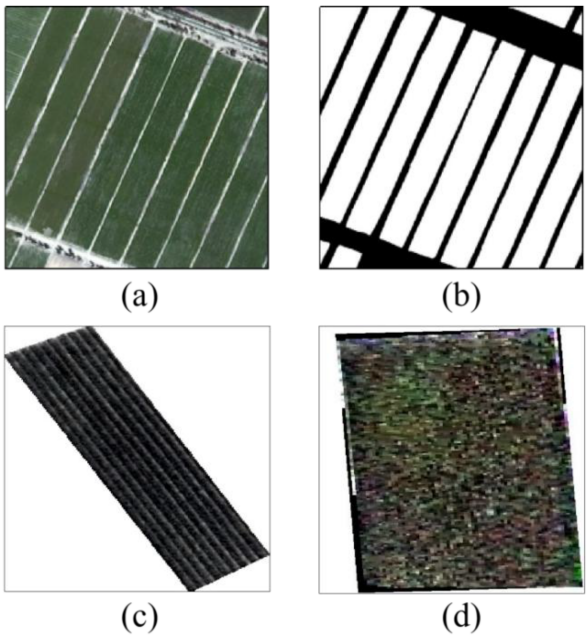

Fig. 6. Training data description. (a) RGB composites of raster data. (b) Segmented parcels. (c) and (d) Samples used for classification, specifically seed maize and common fields, respectively.

fields. Fig. 6(c) and (d) shows samples of seed maize fields and common maize fields, respectively.

B. Experimental Design

In this section, we describe how we conducted experiments and verified the effectiveness of the improved model and HoSS.

TABLE II
TRADITIONAL FEATURE SETS USED FOR COMPARING THE ACCURACY OF SEED MAIZE FIELD IDENTIFICATION

Feature type	Feature
Optical features	Blue
	Green
	Red
	Near infrared (NIR)
Index features	Difference vegetation index (DVI)
	Normalized Difference Vegetation Index (NDVI)
	Enhanced Vegetation Index (EVI)
	Ratio Vegetation index (RVI)
Textural features	GLCM-Contrast
	GLCM-Dissimilarity
	GLCM-Homogeneity
	GLCM-Energy
	GLCM-Correlation
	GLCM-Mean
	GLCM-Entropy
	Local Binary Pattern (LBP)

For field segmentation, to verify the effectiveness of the model improvement, we compared the segmentation accuracy of the model before and after the improvement, and at the same time added a traditional machine learning classifier, the random forest model [22], to perform the comparison between the machine learning model and the deep learning model. For maize field recognition, we compare the performance of HoSS with other feature sets in different classifiers. The feature set consists of optical, index, and texture features, and Table II details the individual features. The machine classifiers used in this study included support vector machine (SVM) [23], random forest

(RF) [24], maximum-likelihood estimation (ML) [25], parallelepiped classifiers (PP), decision tree (DT) [26], [27], and K-nearest neighbors (KNN) [28], and deep learning classifiers included ConvNeXt [29] and Mobile-ViT [30].

Four vegetation indices, namely DVI, NDVI, EVI, and RVI, as classification features. The formula for generating index features is as follows:

$$\mathrm{DVI} = \mathrm{NIR} - R \tag{7}$$

$$\mathrm{NDVI} = (\mathrm{NIR} - R)/(\mathrm{NIR} + R) \tag{8}$$

$$\mathrm{EVI} = (\mathrm{NIR} - R)/(\mathrm{NIR} + 6 \times \mathrm{R} - 7.5 \times \mathrm{B} + 1) \times 2.5 \tag{9}$$

$$\mathrm{RVI} = \mathrm{NIR}/R. \tag{10}$$

The primary texture features used in this study were generated by the GLCM (11), a statistical method proposed by Haralick et al. [31], and a local binary pattern (LBP) [32]. GLCM reflects the combined information on the direction of change, the magnitude of change, and the gray level of the image grayscale [33], and we have selected seven of these GLCM features to be used as inputs to the classification model.

$$\begin{cases} \mathrm{Mean} = \frac{\sum_i \sum_j P(i,j)*i}{n^2} \\ \mathrm{Contrast} = \sum_i \sum_j (i-j)^2 P(i,j) \\ \mathrm{Dissmilarity} = \sum_i \sum_j |i-j| P(i,j) \\ \mathrm{Homogeneity} = \sum_i \sum_j \frac{1}{(i-j)^2+1} P(i,j) \\ \mathrm{Energy} = \sum_i \sum_j P(i,j)^2 \\ \mathrm{Correlation} = \frac{\sum_i \sum_j (i-\mu_i)(j-\mu_j) P(i,j)}{\sigma_i \sigma_j} \\ \mathrm{Entropy} = \sum_i \sum_j P(i,j) \log_2 P(i,j) \end{cases} \tag{11}$$

where i and j represent its position in the matrix and $P(i, j)$ represents the pixel value of the image here. n represents the number of pixels, μ represents the average value of pixels, and σ represents the variance.

LBP is a sequence of 0 and 1 formed by comparing the size between the surrounding pixels and the central pixel. This binary series is then converted into a decimal value (12). This feature is thought to be effective in describing the grayscale variations around the central point. A rotation-invariant LBP algorithm was finally adopted in this study to compute image features [34], by continuously changing the starting position of the binary series and obtaining the smallest value to be returned as the LBP feature value.

$$\mathrm{LBP} = \sum_{p=1}^{8} s(g(p) - g_0) 2^p \tag{12}$$

where $g(p)$ represents the pixels around the central point g_0, the $s()$ function is a binary step function, returns 1 if $g(p)$ is greater than g_0, and 0 otherwise. Multiplying by 2^P is done to convert the binary representation into a decimal value. Traverse the eight pixels around g_0 in a clockwise direction, different starting points can get different LBP values, and we choose the smallest LBP value as the final value.

The method for using traditional features for classification is shown in Fig. 7. According to the aforementioned algorithm, we generated the feature images, then the feature images were segmented into four blocks, and the grayscale histogram of each block was calculated. These histograms were converted into vectors and then concatenated. The feature vectors were input into the machine learning models SVM, KNN, RF, PP, ML, and DT for classification. The feature maps were fed into the deep learning models, i.e., Mobile-ViT and ConvNeXt, for classification.

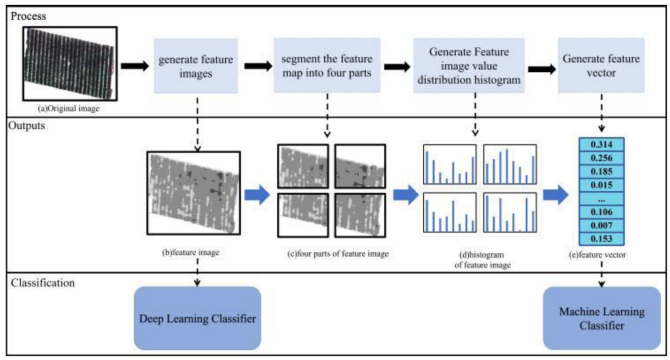

Fig. 7. Process of generating features and applying them to the classifiers.

In single-feature classification experiments, we verify the effectiveness of HoSS by comparing its accuracy with the above features in multiple classifiers. For the classification experiments with multifeature combinations, we analyzed the effectiveness of HoSS features by the difference in accuracy before and after the inclusion of HoSS features. The optimal feature dataset was determined by the optimal index factor (OIF) [35]. OIF selects the best combination of features by considering the standard deviation within an image and the correlation between different feature images. The standard deviation shows the amount of information within the images, whereas the correlation coefficient shows the level of redundancy between the images.

$$\mathrm{OIF} = \sum_{i=1}^{n} S_i \Big/ \sum_{j=1}^{n} |R_{ij}|. \tag{13}$$

In (13), S_i represents the standard deviation of the ith feature, and R_{ij} represents the correlation coefficient between the ith and jth features.

C. Accuracy Evaluation Method

For image segmentation, we compared the accuracy of the improved U^2-net model with the original U^2-net, random forest model, SVM, and KNN. We used four original bands to input the models, and both the training and test sets were kept consistent. Table III lists the accuracy metrics we used, some of which are for boundaries. Based on the principles of boundary intersection over union (IOU) [36], the boundary omission rate and the boundary redundancy rate were proposed to be used as evaluation metrics for assessing boundary accuracy. Boundary IOU is obtained by calculating the IOU of the predicted boundary and the ground truth boundary. The boundary redundancy rate represents the ratio of misclassified boundaries to true boundaries, whereas the boundary omission rate indicates the ratio of missed boundaries to true boundaries (14). The intersection of

TABLE III
EVALUATION METRICS USED IN THE SEGMENTATION AND CLASSIFICATION MODELS IN THIS STUDY

Metrics	Evaluation metrics
Segmentation metrics	User accuracy
	Producer accuracy
	Overall accuracy
	Intersection over union
	Boundary intersection over union
	Boundary redundancy rate
	Boundary omission rate
Classification metrics	Overall accuracy

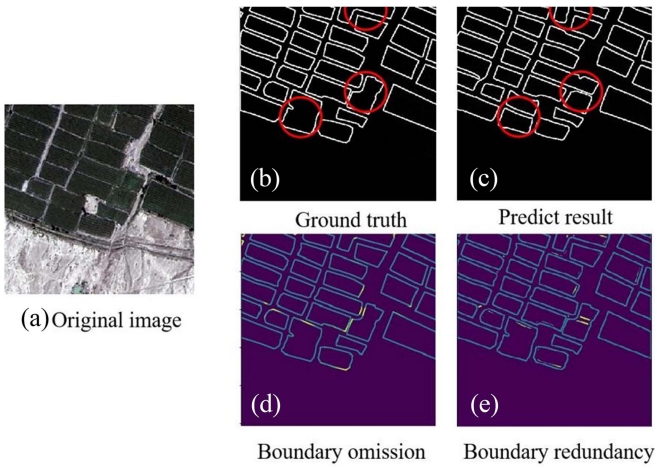

Fig. 8. Display of boundary redundancy and omission. (a) Original image. (b) Ground truth. (c) Predict result. (d) Boundary omission. (e) Boundary redundancy. Top Right: The red circles mark the prediction errors. Lower Right: Highlight redundant and missing boundaries.

the predicted and true boundaries indicates the fraction correctly predicted, with lower values of both metrics indicating more accurate boundary predictions. In Fig. 8, the boundary omission and redundancy parts have been highlighted with red circles and lines of different colors. For the classification experiments, we evaluated the effect of different features and classifiers on classification accuracy using overall accuracy. All accuracy metrics are listed in Table III.

$$\begin{cases} \text{Boundary Intersection Over Union} = \frac{\text{Pred}\cap\text{Truth}}{\text{Pred}\cup\text{Truth}} \\ \text{Boundary redundancy rate} = \frac{\text{Truth}-(\text{Pred}\cap\text{Truth})}{\text{Truth}} \\ \text{Boundary omission rate} = \frac{\text{Pred}-(\text{Pred}\cap\text{Truth})}{\text{Truth}} \end{cases}. \quad (14)$$

D. Comparison of the Improved Model With Boundary Loss With Other Models

We compared the segmentation accuracy using the improved U^2-net model with the original U^2-net and the commonly used machine learning classifiers including random forest, SVM, and KNN (see Fig. 9). All models were trained using the same training and testing datasets. Table IV shows the specific accuracy of each model.

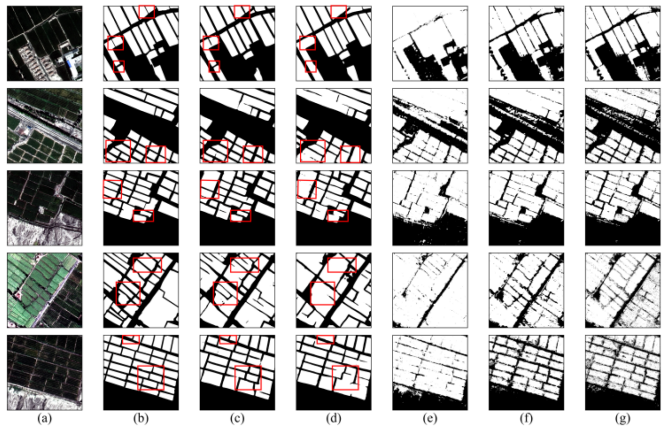

Fig. 9. Comparison of segmentation accuracy using different algorithms. (a) Original image. (b) Ground truth. (c) Segmentation maps were generated by applying an improved U^2-net. (d) Original U^2-net. (e) Random forest classifier. (f) Support vector machine. (g) K-nearest neighbor. The red boxes pointed the boundary difference before and after the U^2-net improvement.

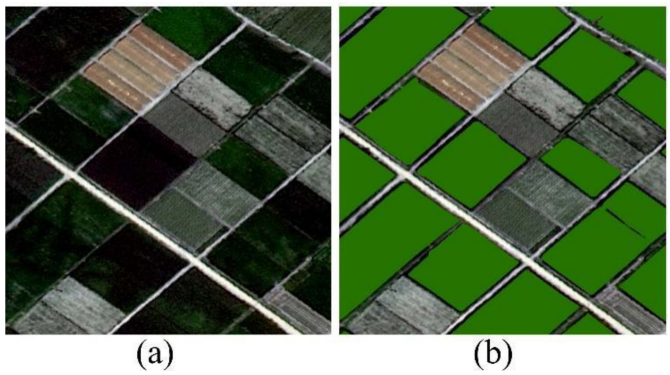

Fig. 10. Parcel segmentation results, including maize fields and nonmaize crop fields. (a) Original image. (b) Segmentation result by U^2-net.

To enhance the model's ability to accurately distinguish between maize and other crops, we precisely outlined maize plots in the sample creation process. Nonmaize farmland was categorized under other land types, and through model backpropagation and parameter updates, the model achieved excellent maize plot recognition capabilities, effectively distinguishing maize from other crops. More detailed classification results are shown in Fig. 10, where it is evident that the maize plots are extracted accurately and exhibit good separation from other crop plots.

E. Comparison of Classification Accuracy of HoSS With Other Features

This study compares the classification accuracy of single features using different machine learning and deep learning classifiers. The selected features and classifiers are described in Section III-B. Table V displays the accuracy of single-feature classification.

In our multifeature combination classification experiments, we first used the OIF index to do feature selection under different

TABLE IV
COMPARISON OF SEGMENTATION ACCURACY BETWEEN THE IMPROVED U^2-NET AND OTHER MODELS

Metrics	Improved U^2-net	Original U^2-net	Random forest classifier	Support vector machine	K-nearest neighbors
User's accuracy	**0.927**	0.911	0.731	0.742	0.781
Producer's accuracy	0.937	0.945	**0.996**	0.966	0.974
Overall accuracy	0.918	**0.922**	0.809	0.804	0.849
Intersection over union	0.853	**0.865**	0.729	0.727	0.742
Boundary intersection over union	**0.450**	0.432	0.131	0.102	0.181
Boundary redundancy rate	**0.151**	0.161	0.317	0.311	0.287
Boundary omission rate	**0.206**	0.261	0.581	0.591	0.504

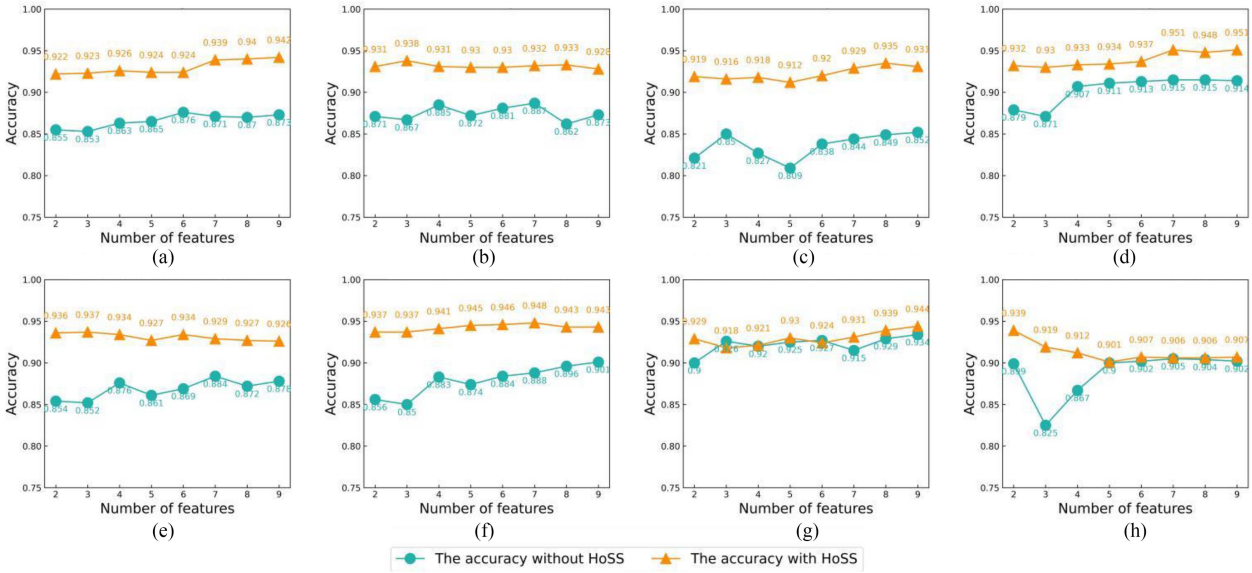

Fig. 11. Orange: Accuracy achieved by different classifiers with feature sets that included HoSS. Green: accuracy achieved by different classifiers with feature sets that did not include HoSS. (a) Support vector machine (SVM). (b) Random forest (RF). (c) Maximum likelihood (ML). (d) Parallel pipe (PP). (e) Decision tree (DT). (f) K-nearest neighbors (KNN). (g) Mobile-ViT. (h) ConvNeXt.

numbers of features and conducted comparison experiments before and after HoSS inclusion in the feature set. Table VI shows the choice of band combinations. To visualize the change in accuracy before and after HoSS feature inclusion, the difference in accuracy is shown in Fig. 11.

HoSS features added to the feature set resulted in an average classification accuracy of 93.7% compared to 89.3% without HoSS. In the above experiments, a total of 64 control experiments were conducted, of which 62 experiments showed an improvement in classification accuracy with the addition of HoSS.

Among the various combinations of classifiers and features, the combination of entropy and HoSS as inputs to the nearest neighbor classifier achieves a high level of accuracy (93.7%), which is not a significant difference compared to the highest experimentally achieved accuracy of 94.8%. In addition, the training time of the KNN classifier is relatively short, and the use of only two features significantly reduces the cost and time of feature generation. Hence, this method was finally selected in this study for the identification of seed maize fields (see Fig. 12).

IV. DISCUSSION

A. *Effect of Improved Loss Function on Segmentation Accuracy*

The boundary accuracy demonstrated better boundary identification for an improved U^2-net model. Our improvements to the model were mainly a new boundary loss function with the lightweight improvement of the model, which achieves a significant reduction in the number of parameters. How can the accuracy of the plot boundaries be improved is also an important issue in the model without losing accuracy. In the

TABLE V
CLASSIFIER'S SINGLE-FEATURE CLASSIFICATION ACCURACY

Feature	SVM	RF	ML	PP	DT	KNN	MobileViT	ConvNext
Band: Blue	0.631	0.758	0.616	0.743	0.685	0.517	0.822	0.820
Band: Green	0.650	0.757	0.653	0.746	0.672	0.500	0.832	0.834
Band: Red	0.598	0.732	0.563	0.700	0.653	0.518	0.848	0.825
Band: NIR	0.650	0.730	0.512	0.704	0.607	0.445	0.773	0.906
Band: Gray	0.648	0.764	0.644	0.742	0.654	0.523	0.833	0.824
NDVI	0.760	0.798	0.736	0.814	0.722	0.555	0.855	0.754
EVI	0.593	0.638	0.637	0.654	0.592	0.317	0.809	0.783
RVI	0.699	0.755	0.657	0.753	0.698	0.549	0.810	0.806
DVI	0.669	0.763	0.646	0.765	0.704	0.459	0.855	0.711
Contrast	0.517	0.570	0.518	0.582	0.524	0.325	0.844	0.810
Dissimilarity	0.525	0.617	0.534	0.618	0.550	0.345	0.781	0.741
Homogeneity	0.706	0.693	0.681	0.746	0.695	0.469	0.823	0.820
Energy	0.664	0.679	0.640	0.705	0.645	0.444	0.847	0.843
Correlation	0.742	0.695	0.706	0.791	0.737	0.656	0.829	0.835
Mean	0.527	0.608	0.534	0.607	0.570	0.332	0.839	0.817
Entropy	0.854	0.860	0.829	0.853	0.793	0.844	0.864	0.918
LBP	0.774	0.794	0.745	0.816	0.761	0.768	0.910	0.895
HoSS	**0.896**	**0.915**	**0.893**	**0.915**	**0.863**	**0.897**	**0.935**	**0.930**

Band (Gray) = 0.3×Band (Red)+0.59×Band (Green)+0.11×Band (Blue).

TABLE VI
BAND COMBINATIONS USED IN ACCURACY ANALYSIS INCLUDE COMBINATIONS OF THE NUMBER OF BANDS BEFORE AND AFTER THE ADDITION OF HOSS

Number of bands	Name of the band used for the combination
2	Entropy + DVI
	Entropy + HoSS
3	Entropy + DVI + NIR
	Entropy + DVI + HoSS
4	Entropy + DVI + NIR + LBP
	Entropy + DVI + NIR + HoSS
5	Entropy + DVI + NIR +LBP + Contrast
	Entropy + DVI + NIR + LBP + HoSS
6	Entropy + DVI + NIR + LBP + Contrast + Red
	Entropy + DVI + NIR + LBP + Contrast + HoSS
7	Entropy + DVI + NIR + LBP + Contrast + Red + Gray
	Entropy + DVI + NIR + LBP + Contrast + Red + HoSS
8	Entropy + DVI + NIR + LBP + Contrast + Red + Gray + Green
	Entropy + DVI + NIR + LBP + Contrast + Red + Gray + HoSS
9	Entropy + DVI + NIR + LBP + Contrast + Red + Gray + Green + Blue
	Entropy + DV I+ NIR + LBP + Contrast + Red + Gray + Green + HoSS

field of remote sensing, the extraction of plot boundaries is particularly important. Correctly extracting and vectorizing plot boundaries is a research direction in precision agriculture. This study has attempted to improve the extraction of plot boundaries by refining the segmentation model's loss function, effectively enhancing the accuracy of extracted farmland boundaries and making initial progress. In situations where the mechanism of deep learning models is difficult to analyze, it is reasonable and effective to artificially improve the loss function, as designing a loss function is an interpretable means of guiding the model through human experiential knowledge. Additionally, the artificial imposition of constraints can also improve the model. For example, it is feasible to use a combination of loss functions and regularization terms to constrain the model's output boundaries. Subsequent research will follow this line of thinking.

TABLE VII
CLASSIFICATION ACCURACY OF A SINGLE FEATURE CLASSIFIER ON TEST SETS FROM OTHER REGIONS

Feature	SVM	RF	ML	PP	DT	KNN	MobileViT	ConvNext
Entropy	0.850	0.843	0.825	0.845	0.753	0.830	0.828	**0.893**
LBP	0.773	0.770	0.708	0.798	0.720	0.755	0.875	0.873
Correlation	0.723	0.698	0.695	0.755	0.728	0.633	0.876	0.803
NDVI	0.633	0.660	0.708	0.790	0.700	0.640	0.808	0.710
HoSS	**0.868**	**0.895**	**0.883**	**0.885**	**0.828**	**0.880**	**0.920**	**0.893**

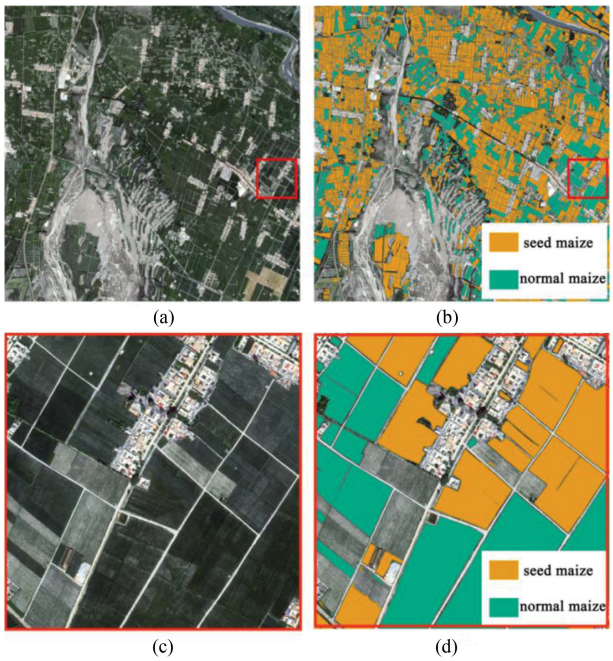

Fig. 12. (a) Single BJ-3 satellite image. (b) Maize identification result. (c) Local area image. (d) Local maize identification result.

The machine learning model generated the worst results. While the user accuracy for random forests reached 99.6%, all other accuracy metrics were lower than those of the deep learning models. It is important to note that the high user accuracy and low producer accuracy of the machine learning model in the binary classification task is due to its tendency to misclassify other land cover types as maize fields. This is due to the spectral similarity of the different features, with some of the trees and black areas in the classified images being misclassified as maize fields.

The improved U^2-net model showed a slight decrease in IOU and overall accuracy, the boundary IOU accuracy increased, and the redundancy rate of boundaries and boundary omission rate decreased. This indicated the effectiveness of the new loss function for boundary prediction. A slight decrease in IOU and producer's accuracy in the improved U^2-net model can be due to the fine segmentation, which resulted in the loss of area at the boundaries of maize fields. However, accurate outlining of maize field boundaries is of major importance for subsequent classification tasks.

We analyzed the impact of the loss function improvement on the model. The original U^2-net segmentation model employed the cross-entropy loss function. However, the concentrated distribution of maize plots results in a category imbalance in the images of the training set, with frequent extremes where most of the area is maize fields or most of the area is nonmaize fields. Cross-entropy loss exhibits clear limitations when dealing with category imbalance because it assumes that all the categories have equal importance, which typically leads to unstable training [37]. Also, this loss function does not fully consider the importance of boundaries. In this study, the new loss function for field segmentation we introduced that combined dice loss function to evaluate the prediction accuracy of the boundary. The dice loss function has good performance in the case of sample imbalance (the boundary pixels account for a few pixels in the overall image), and the experimental results also show that the boundary accuracy is improved.

B. Ability of HoSS Features in Multiple Classification Situations

The basic principle of HoSS is to extract the slope distribution of the stripe statistics to determine whether it is a seed maize field or not, the experimental results show that the highly consistent distribution of the stripe inside the seeded maize fields can be used as the best classification feature. The experimental results show that the highly consistent stripe distribution inside the seed maize fields can be used as the best classification feature. Compared to the traditional classification methods using textural, spectral, and vegetation index features, our proposed feature has a stronger ability to distinguish between seed maize fields and common maize fields.

For single-feature classification, the ability of HoSS to identify seed maize fields is shown by box plots. HoSS brings even more significant accuracy gains in machine learning classifiers. Overall, an average classification accuracy of 90.5% can be achieved when using a single HoSS feature, while the average maximum accuracy that can be achieved using each classifier is 85.1% when using other classical features. When machine learning classifiers, HoSS provides an average improvement of 5.76% in classification accuracy compared to other classical features, whereas these results show an average improvement of 1.85% for deep learning classifiers.

There are also large differences in the accuracy of different classifiers, with deep learning classifiers outperforming machine learning classifiers. When using HoSS features for classification, the deep learning model can achieve a maximum classification accuracy of 93.5%, with an average classification accuracy of 3.65% higher than that of machine learning classifiers. In

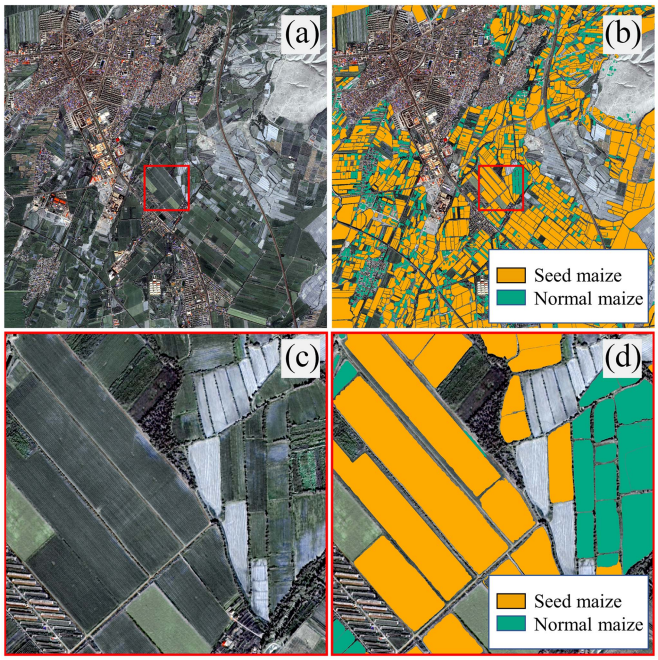

Fig. 13. Verification results of seed maize classification in Huocheng County. (a) Single BJ-3 satellite image. (b) Maize identification result. (c) Local area image. (d) Local maize identification result.

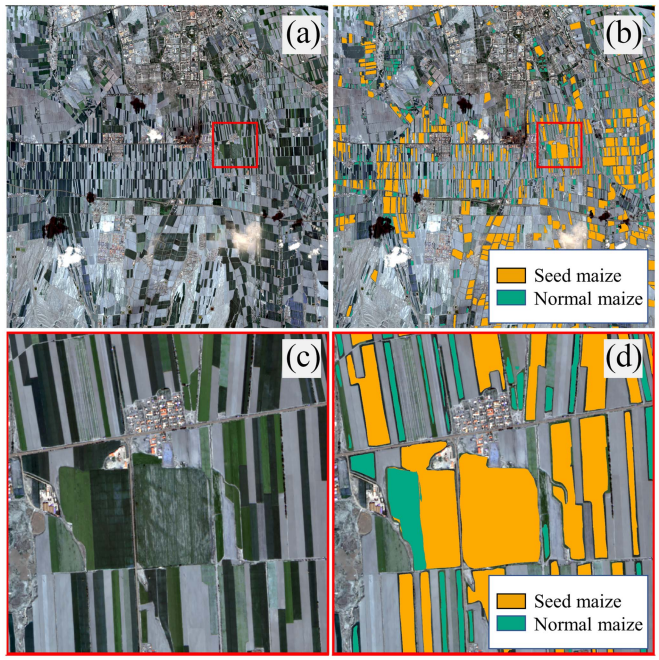

Fig. 14. Verification results of seed maize classification in Qitai County. (a) Single BJ-3 satellite image. (b) Maize identification result. (c) Local area image. (d) Local maize identification result.

addition, when the deep learning classifier uses other traditional features, the maximum accuracy can exceed 91%, indicating that deep learning classifiers have superior capabilities in single-feature approaches, especially when using HoSS features.

The increase in the number of features also has an impact on the classification accuracy, with most classifiers slowly increasing in accuracy as more features are added, and this accuracy improvement is greatest when increasing from a single band to two bands for classification. We found that most machine learning models, without the need for large amounts of training time, can effectively classify seed maize fields with similar accuracy as deep learning classifiers. As for the deep learning models, the ConvNeXt model's accuracy instead decreases with the increase of features and eventually stabilizes at around 0.905. In contrast, the Mobile-ViT model, which incorporates an attentional mechanism, steadily maintains accuracy while adding more features. This may be attributed to the fact that the attention mechanism is better able to identify the important parts of the features while ignoring the redundant parts. At the same time, We have observed that the inclusion of the HoSS feature in the deep learning MobileViT model does not significantly improve accuracy, and there are cases where adding the HoSS feature actually leads to worse results than not including it. Our initial hypothesis is that the MobileViT model introduces an attention mechanism that has a high discriminative ability for simple stripe textures. Other features discovered in the feature extraction layer are already superior to the HoSS feature, suggesting that the impact of adding HoSS to the model is minimal.

C. HoSS Feature Generalization Evaluation Experiment

To validate the universality of the HoSS method, we established two new experimental areas in Huocheng County and Qitai County in Xinjiang Uygur Autonomous Regions, China. Remote sensing data from Gaofen-7 between July 25 and August 25, 2022, was used, and a total of 400 corn plots were visually interpreted to create the test samples. The features Entropy, LBP, correlation, and NDVI were compared with HoSS, based on their previous performance rankings. The specific results are shown in Table VII, and the classification results are shown in Figs. 13 and 14.

It can be observed that in other regions, the HoSS features still work well. The texture features perform similarly to the experimental accuracy in the Ganzhou area. However, the transferability of NDVI features is poor. This may be due to differences in corn varieties in different regions, leading to significant NDVI variations. Another possible reason could be the differences in the band ranges between the GF-7 sensor and the BJ-3 sensor, resulting in lower classification accuracy.

V. Conclusion

In this study, a two-step approach of segmentation plus classification was used to accurately identify seed maize fields in the Ganzhou region.

In the segmentation step, a plot segmentation loss function was designed to improve the segmentation U^2-net model and enhance the boundary extraction capability of the model.

In the classification step, a feature called the HoSS feature was constructed for stripe texture analysis and showed superior performance in classifying seed maize fields. The HoSS feature based on a statistical analysis of stripe slopes has a random slope distribution histogram for common maize fields and a concentrated slope histogram for maize seed fields. The results of the study show that this feature alone or in combination with other features performs excellently in terms of classification

accuracy. Furthermore, since this texture feature is not limited to seed maize fields and is prevalent in other classification themes, the application of this feature can be extended to texture classification and linear feature detection.

REFERENCES

[1] Y. Zhao et al., "Modelling water/heat transfer and crop growth under film mulching condition in a seed–maize field," *Agricultural Forest Meteorol.*, vol. 340, 2023, Art. no. 109616.

[2] H. Wright, "Commercial hybrid seed production," in *Hybridization of Crop Plants*. Madison, WI, USA: Amer. Soc. Agron., 1980, pp. 161–176.

[3] C. Gómez, J. C. White, and M. A. Wulder, "Optical remotely sensed time series data for land cover classification: A review," *ISPRS J. Photogramm. Remote Sens.*, vol. 116, pp. 55–72, 2016.

[4] M. Weiss, F. Jacob, and G. Duveiller, "Remote sensing for agricultural applications: A meta-review," *Remote Sens. Environ.*, vol. 236, 2020, Art. no. 111402.

[5] L. Zhang et al., "Identification of seed maize fields with high spatial resolution and multiple spectral remote sensing using random forest classifier," *Remote Sens.*, vol. 12, no. 3, 2020, Art. no. 362.

[6] T. Ren et al., "Early identification of seed maize and common maize production fields using Sentinel-2 images," *Remote Sens.*, vol. 12, no. 13, 2020, Art. no. 2140.

[7] J. Yao et al., "The classification method study of crops remote sensing with deep learning, machine learning, and Google Earth Engine," *Remote Sens.*, vol. 14, no. 12, 2022, Art. no. 2758.

[8] Z. Chao et al., "Seed maize identification based on texture analysis of GF remote sensing data," *Trans. Chin. Soc. Agricultural Eng.*, vol. 32, pp. 183–188, 2016.

[9] L. Zhe et al., "Seed maize identification based on time-series EVI decision tree classification and high resolution remote sensing texture analysis," *Trans. Chin. Soc. Agricultural Mach.*, vol. 46, pp. 321–327, 2015.

[10] C. Zhang et al., "Identification method of seed maize plot based on multi-temporal GF-1 WFV and Kompsat-3 texture," *Trans. Chin. Soc. Agricultural Mach.*, vol. 50, pp. 163–168, 2019.

[11] X. Qin et al., "U^2-Net: Going deeper with nested U-structure for salient object detection," *Pattern Recognit.*, vol. 106, 2020, Art. no. 107404.

[12] X. Wei et al., "Building outline extraction directly using the U^2-net semantic segmentation model from high-resolution aerial images and a comparison study," *Remote Sens.*, vol. 13, no. 16, 2021, Art. no. 3187.

[13] Z. Ye et al., "Extraction of olive crown based on UAV visible images and the U^2-net deep learning model," *Remote Sens.*, vol. 14, no. 6, 2022, Art. no. 1523.

[14] Z. Zou et al., "Extraction of aquaculture ponds along coastal region using U^2-net deep learning model from remote sensing images," *Remote Sens.*, vol. 14, no. 16, 2022, Art. no. 4001.

[15] L. Sifre and S. Mallat, "Rigid-motion scattering for texture classification," 2014, *arXiv:1403.1687*.

[16] A. Bokhovkin and E. Burnaev, "Boundary loss for remote sensing imagery semantic segmentation," in *Proc. Int. Symp. Neural Netw.*, 2019, pp. 388–401.

[17] F. Milletari, N. Navab, and S.-A. Ahmadi, "V-Net: Fully convolutional neural networks for volumetric medical image segmentation," in *Proc. 4th Int. Conf. 3D Vis.*, 2016, pp. 565–571.

[18] X. Li et al., "Dice loss for data-imbalanced NLP tasks," 2019, *arXiv:1911.02855*.

[19] F. Chollet, "Xception: Deep learning with depthwise separable convolutions," in *Proc. IEEE Conf. Comput. Vis. Pattern Recognit.*, 2017, pp. 1800–1807.

[20] F. Zhong et al., "Eco-efficiency of oasis seed maize production in an arid region, Northwest China," *J. Cleaner Prod.*, vol. 268, 2020, Art. no. 122220.

[21] W. Song and Y. Zhang, "Expansion of agricultural oasis in the Heihe River Basin of China: Patterns, reasons and policy implications," *Phys. Chem. Earth, Parts A/B/C*, vol. 89, pp. 46–55, 2015.

[22] F. Schroff, A. Criminisi, and A. Zisserman, "Object class segmentation using random forests," in *Proc. Brit. Mach. Vis. Conf.*, 2008, pp. 1–10.

[23] C. Cortes and V. Vapnik, "Support-vector networks," *Mach. Learn.*, vol. 20, pp. 273–297, 1995.

[24] L. Breiman, "Random forests," *Mach. Learn.*, vol. 45, pp. 5–32, 2001.

[25] R. A. Fisher, "On the mathematical foundations of theoretical statistics," *Philos. Trans. Roy. Soc. London. A, Math. Phys. Character*, vol. 222, no. 594–604, pp. 309–368, 1922.

[26] E. B. Hunt, J. Marin, and P. J. Stone, *Experiments in Induction*. New York, NY, USA: Academic, 1966.

[27] J. R. Quinlan, "Induction of decision trees," *Mach. Learn.*, vol. 1, pp. 81–106, 1986.

[28] T. Cover and P. Hart, "Nearest neighbor pattern classification," *IEEE Trans. Inf. Theory*, vol. IT-13, no. 1, pp. 21–27, Jan. 1967.

[29] Z. Liu, H. Mao, C.-Y. Wu, C. Feichtenhofer, T. Darrell, and S. Xie, "A ConvNet for the 2020s," in *Proc. IEEE/CVF Conf. Comput. Vis. Pattern Recognit.*, 2022, pp. 11966–11976.

[30] S. Mehta and M. Rastegari, "MobileViT: Light-weight, general-purpose, and mobile-friendly vision transformer," 2021, *arXiv:2110.02178*.

[31] R. M. Haralick, K. Shanmugam, and I. H. Dinstein, "Textural features for image classification," *IEEE Trans. Syst., Man, Cybern.*, vol. SMC-3, no. 6, pp. 610–621, Nov. 1973.

[32] T. Ojala, M. Pietikainen, and D. Harwood, "Performance evaluation of texture measures with classification based on Kullback discrimination of distributions," in *Proc. 12th Int. Conf. Pattern Recognit.*, 1994, vol. 1, pp. 582–585.

[33] M. Hall-Beyer, "GLCM texture: A tutorial," National Council Geographic Information and Analysis Remote Sensing Core Curriculum, vol. 3, no. 1, p. 75, 2000.

[34] T. Ojala, M. Pietikainen, and T. Maenpaa, "Multiresolution gray-scale and rotation invariant texture classification with local binary patterns," *IEEE Trans. Pattern Anal. Mach. Intell.*, vol. 24, no. 7, pp. 971–987, Jul. 2002.

[35] P. Chavez, G. L. Berlin, and B. Lynda, "Statistical method for selecting Landsat MSS ratios," *J. Appl. Photograph. Eng.*, vol. 8, pp. 23–30, 1982.

[36] B. Cheng, R. Girshick, P. Dollár, A. C. Berg, and A. Kirillov, "Boundary IoU: Improving object-centric image segmentation evaluation," in *Proc. IEEE/CVF Conf. Comput. Vis. Pattern Recognit.*, 2021, pp. 15329–15337.

[37] T.-Y. Lin, P. Goyal, R. Girshick, K. He, and P. Dollár, "Focal loss for dense object detection," *IEEE Trans. Pattern Anal. Mach. Intell.*, vol. 42, no. 2, pp. 318–327, Feb. 2020.

Yunqi Shen received the B.S. degree in geographic information science from Anhui University, Hefei, China, in 2021. He is currently working toward the Ph.D degree in cartography and geography information systems from the University of Chinese Academy of Sciences, Beijing, China.

His research interests include deep learning modeling for the extraction of farm facility elements and extraction of canals, farmland, and field roads.

Hongyan Wang received the B.Sc. degree in soil and water conservation and desertification combating from Shandong Agricultural University, Tai'an, China, in 2008, and the Ph.D. degree in forest management from the Chinese Academy of Forestry, Beijing, China, in 2013.

She is currently an Assistant Researcher with the Aerospace Information Research Institute, Chinese Academy of Sciences, Beijing, China. Her research interests include crop mapping, application of remote sensing in precision agriculture, and monitoring and evaluation of land degradation.

Yuan Zhang received the Ph.D. degree in geography from the University of Utah, Salt Lake City, UT, USA, in 2013.

From 2013 to 2016, she was a postdoctoral researcher with the Institute of Remote Sensing and Geographic Information Systems, Peking University. She is currently an Associate Professor with the Aerospace Information Research Institute, Chinese Academy of Sciences, Beijing, China. Her research interests include agro-disaster monitoring, phenological modeling, and urban environment analysis integrating remote sensing and social sensing data.

Xin Du received the Ph.D. degree in cartography and geographical information systems from the Institute of Remote Sensing Applications, Chinese Academy of Sciences, Beijing, China, in 2011.

He is currently an Associate Professor with the Aerospace Information Research Institute, Chinese Academy of Sciences. His research interests include remote sensing Big Data intelligent modeling, smart agriculture and remote sensing, and ecological and environmental remote sensing.

Qinghan Dong received the B.S. degree in chemistry and Ph.D. degree in biochemistry from Universite Libre de Bruxelles, Brussels, Belgium, in 1985 and 1991, respectively.

He is currently a Senior Scientist with the Flemish Institute of Technological Research (VITO), Mol, Belgium. His current research focuses on remote sensing applications in agriculture and environment domains.

Qiangzi Li received the Ph.D. degree in cartography and geographical information systems from the Institute of Remote Sensing Applications, Chinese Academy of Sciences, Beijing, China, in 2008.

He is currently a Professor with the Aerospace Information Research Institute, Chinese Academy of Sciences. His research interests include remote sensing identification and area estimation of crops, remote sensing estimation of grain production capacity, analysis of agricultural disasters and environmental conditions using remote sensing, agricultural informatization, ecological and environmental remote sensing, and remote sensing applications in public security.

Yueting Wang received the B.S. degree in geographic information systems from Ludong University, Yantai, China, in 2012, and the M.S. and Ph.D. degrees in forestry equipment and informatization from Beijing Forestry University, Beijing, China, in 2015 and 2022, respectively.

Since 2022, she has been a postdoctoral scholar with the Aerospace Information Research Institute, Chinese Academy of Sciences, Beijing. Her research interests include agricultural and forestry resources and ecological environment remote sensing monitoring and spatial prediction.

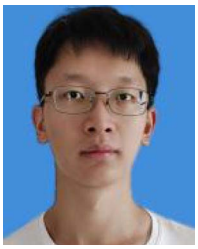

Sichen Zhang received the B.S. degree in surveying and mapping engineering from the China University of Mining and Technology, Xuzhou, China, in 2021. He is currently working toward the M.S. degree in cartography and geography information systems from the University of Chinese Academy of Sciences, Beijing, China, in 2024.

His research interests include the inversion of vegetation parameters and remote sensing of agriculture.

Yong Dong received the B.S. degree in geographic information science from Peking University, Beijing, China, in 2022. He is currently working toward the Ph.D. degree in cartography and geographic information systems with the University of Chinese Academy of Sciences, Beijing.

His research interests include crop remote sensing parameter inversion and precision agriculture.

Jing Xiao received the bachelor's degree in geographic information systems from Northeast Normal University, Changchun, China, in 2022. She is currently working toward the master's degree in cartography and geographic information systems with the University of Chinese Academy of Sciences, Beijing, China.

Her current research focuses on the field of agricultural remote sensing.

Jingyuan Xu received the B.S. degree in geographical information science from China Agricultural University, Beijing, China, in 2022. She is currently working toward the M.S. degree in cartography and geography information systems from the University of Chinese Academy of Sciences, Beijing.

Her research interests include crop yield estimation, data assimilation, and cropland productivity assessment.

Sifeng Yan received the B.S. degree in remote sensing science and technology from the China University of Geosciences, Wuhan, China, in 2023. He is currently working toward the Ph.D. degree in cartography and geography information systems from the Aerospace Information Research Institute, University of Chinese Academy of Sciences, Beijing, China.

His research interests include agricultural remote sensing and yield estimation.

Shuguang Gong received the B.S. degree in geographic information science from Zhengzhou University, Zhengzhou, China, in 2023. He is currently working toward the Ph.D. degree in cartography and geography information systems from the Aerospace Information Research Institute, University of Chinese Academy of Sciences, Beijing, China.

His research interests include agricultural remote sensing and yield estimation.

Haoxuan Hu received the B.S. degree in remote sensing science and technology from Sun Yat-sen University, Guangzhou, China, in 2023. He is currently working toward the M.S. degree in cartography and geography information systems from the University of Chinese Academy of Sciences, Beijing, China.

His current research focuses on agricultural parameter retrieval.